Electrochimica Acta 376 (2021) 137989

Contents lists available at ScienceDirect

Electrochimica Acta

journal homepage: www.elsevier.com/locate/electacta

Enhanced supercapacitive properties of hydrohausmannite by *in-situ* polymerization of polypyrrole

Yan Zhuang[a], Qiangqiang Niu[a], Wenjie Wu[a], De Yan[a,b,*], Juanjuan Huang[a,*], Shanglong Peng[a,d,*], Jun Wang[a], Renfu Zhuo[a], Zhiguo Wu[a,b], Guozhong Cao[a,c,*]

[a] School of Physical Science and Technology, Lanzhou University, 730000, China
[b] Institute of Nanomaterials Application Technology, Gansu Academy of Science, Lanzhou 730000, China
[c] Department of Materials Science and Engineering, University of Washington, -2120, Seattle, WA 98195, United States
[d] College of Science, Key Laboratory of Ecophysics, Department of Physics, Shihezi University, Xinjiang 832003, China

ARTICLE INFO

Article history:
Received 12 September 2020
Revised 29 January 2021
Accepted 16 February 2021
Available online 22 February 2021

Keywords:
Performance promotion
Negative potential
Polymerization time
Multi-ion storage

ABSTRACT

The main limitations of manganese oxides as supercapacitor electrodes in negative potential (-0.5~0.5 vs saturated calomel electrode (SCE)/V) are irreversible redox reaction, phase transformation and low conductivity. Phase transformation to birnessite induced by irreversible Na^+ intercalation was found in hydrohausmannite (abbreviated as MO) electrode, accompanied by Mn^{2+} dissolution and structural collapse. Polypyrrole (PPy) film was synthesized on the surface of MO by a simple and timesaving *in-situ* polymerization method with the assistance of H^+ and Mn^{4+}. The PPy/MO electrode shows a promoted specific capacitance (183 F g^{-1} at 0.5 A g^{-1}), enhanced rate capability (91 F g^{-1} at 10 A g^{-1}, about 10 times of MO), and excellent cycling stability (93.7% capacitance retention after 1000 cycles at 10 A g^{-1}). The performance enhancement mechanism after coated by PPy film is investigated. Firstly, PPy films with appropriate polymerization time (or thickness) can allow H^+ to pass and block Na^+, so the irreversible phase transformation of MO is hindered and the structure and morphology of electrode is protected. Secondly, PPy film can also prevent Mn^{2+} from dissolving into electrolyte, so the disproportionation reaction is suppressed and cycling stability is promoted. Thirdly, PPy film can improve the conductivity of the electrode, which greatly accelerates the charge transfer process and enhances the rate capability. Fourthly, besides cations (H^+ and Na^+), anions (SO_4^{2-} and P-toluene sulfonic (p-TS^-)) also participate in energy storage process after coated by PPy, so the specific capacitance is also promoted.

1. Introduction

Supercapacitors, also called the electrochemical capacitors, attracted a large number of researchers' interests on account of their high power density, promising long circle stabilities and fast charging/ discharging rate [1–3]. According to the equation $E = 1/2CV^2$, the energy density (E) of supercapacitor was related to the specific capacitance (C) and the cell voltage (V) [4]. Therefore, to develop superior supercapacitors, electrode material needed to provide higher specific capacitance and wider cell voltage. The common supercapacitor electrode material mainly includes: carbon materials (e.g., activated carbon, carbon nanotubes, carbon nanofibers and graphene), conducting polymers (e.g., PPy, polyaniline, polythiophene and their corresponding derivatives) and transition metal oxides (e.g., MnO_x, RuO_2, Co_3O_4, V_2O_5, SnO_2 and IrO_2) [5–12]. Among these electrode materials, manganese oxides/oxyhydroxides (e.g., MnO_2, Mn_3O_4, Mn_2O_3, MnOOH) have been extensively researched because of their low cost, high theoretical capacity and environment friendliness [13–17]. Hydrohausmannite, a mixed phase of γ-Mn_3O_4 and β-MnOOH, is promising electrode material for supercapacitors which has been previously reported, but corresponding researches are rarely seen in literature. Yan et al. fabricated hydrohausmannite plates as supercapacitors electrode material by hydrothermal method, which showed a high specific capacitance of 224.4 F g^{-1} (potential window at 0~0.8 vs SCE/V, 1 mol dm^{-3} $NaSO_4$ as the electrolyte) and good rate capability [18]. Liang et al. synthesized hydrohausmannite nanoplates electrode by one-step solvothermal method and got a high specific capacity of 215 F g^{-1} (potential window at 0~0.8 vs SCE/V, 3 mol dm^{-3} KOH as the electrolyte) [18,19].

As a typical conducting polymer, PPy possesses good electrical conductivity due to its π-conjugation throughout the molec-

* Corresponding authors.
E-mail addresses: yand@lzu.edu.cn (D. Yan), huangjj@lzu.edu.cn (J. Huang), pengshl@lzu.edu.cn (S. Peng), gzcao@u.washington.edu (G. Cao).

https://doi.org/10.1016/j.electacta.2021.137989
0013-4686/

ular chain [20]. And PPy is relatively ease to be synthesized by chemical processes with low cost, and has low environmental toxicity [21]. However, the cycle stability of PPy was barely satisfactory due to swelling and shrinking during charging and discharging processes [22]. Fu et al. synthesize a high-performance PPy nanowire network and Kumar et al. fabricate a PPy/carbon composite electrode, but the capacitance was degraded over 10% after 1000 cycles [23,24]. To get a higher performance PPy, researchers have made a lot of studies on the effects of dopants and found that PPy doped with P-toluene sulfonic acid (p-TSA) shows excellent electrochemical performance since p-TSA can notably raise its conductivity [25–27].

In positive potential region, generally 0~1.0 vs SCE/V, the mechanism of performance fading is widely investigated and considered to be low ion transfer rate, low rate capability and irreversible phase transformation seriously [28]. However, for some manganese oxides electrodes, the capacitance deterioration mainly occurred in negative potential region, and the corresponding mechanism is rarely investigated, especially for hydrohausmannite. Up to now, the reasons of manganese oxides electrode performance deterioration in negative region are still controversial. Sopčić et al. believed that the irreversible phase transformation from MnO_2 to Mn_2O_3 caused the decrease of capacitance [29]. Ataherian et al. thought that the reduction of Mn ions and dissolution mechanism of MnO_2 at negative potentials along with the morphological reconstruction lead to the issue [30]. Hsieh et al. ascribed this phenomenon to the irreversible charge transfer process, which leading to the decrease of available active sites during the energy storage process [31].

To enhance the performance of pure manganese oxides electrodes, many researchers combined manganese oxides with conductive materials, such as carbon nanosheet [32], carbon nanotubes [33], graphene [34] and conducting polymers [35]. Yang et al. have prepared self-supported polyaniline/MnO_2 nanowire network sponge as a binder free electrode, which got a high specific capacitance of 344F g^{-1} [36]. Pintu Sen et al. designed a composite electrode by combining reduced graphene oxide, 3,4-ethylene-dioxythiophene and MnO_2 and found high capacitance value of 345F g^{-1} [37]. Compared with other conducting polymers, PPy is a better composite material for the pseudocapacitive charge storage because of the feasibility of anions and cations dual doping that occurs both positive and negative potentials [38]. Many researches have made MnO_2/PPy composite electrodes materials and found that PPy can obviously raise the capacitance and cycling stability. He et al. constructed hierarchically porous PPy nanowires/MnO_2 core/shell nanostructure and got a high specific capacitance of 276 F g^{-1} at 2A g^{-1} [39]. Sharma et al. synthesized the MnO_2 embedded PPy nanocomposite thin film electrodes which have a good cycling stability [39,40]. Besides, Zhu et al. and Bi et al. demonstrated that the PPy film can provide the protection of electrode structures and selectively pass the cations from electrolyte to the internal of electrode [41,42].

However, these improved performances of composite electrodes involving conducting polymers were obtained in positive potential region. The energy storage mechanism of MO and MO/PPy composite electrodes under negative potentials still need to be further explored.

In this study, to investigate the supercapacitive properties and energy storage mechanism of MO electrode at negative potentials (−0.5~0.5 vs SCE/V), we prepared MO and MO/PPy electrodes by electrodeposition and its combination with *in-situ* polymerization method, respectively. The PPy/MO electrodes presented more stable capacitive behaviors compared with the pure MO electrode. These electrodes are examined and characterized by scanning electron microscope (SEM), transmission electron microscope (TEM), X-ray photoelectron spectrometer (XPS), X-ray diffraction (XRD), Raman spectrum and a series of electrochemical measurement. The mechanism for deterioration of MO and the performance improvement after coated by PPy film is discussed in detail. We expect that this investigation could provide new sights into broadening the working potential window of MO electrode and enhance the understanding of energy storage mechanisms.

2. Experimental

2.1. Pretreatment of carbon cloth

Carbon cloth (CC) was prepared by a hydrophilic treatment to remove the oxide layer on the surface. Specifically, a piece of CC (1 × 1.5 cm^2) was cleaned using acetone, ethanol, and ultrapure water for 30 min in turn. The hydrophilic treatment was carried out in three-electrode system in H_2SO_4 solution with SCE as reference electrode and platinum plate as counter electrode. The electrochemical process was performed on the electrochemical workstation (CHI660E, CH Instruments Inc., Shanghai) under a constant potential of 3 vs SCE/V for 600 s. The as-prepared CCs were washed by ultrapure water for several times and dried at 60 °C for 10 h.

2.2. Synthesis of manganese oxide electrode

MO electrode was synthesized under a galvanostatic electrodeposition process. Briefly, a solution containing sodium sulfate (0.1 mol dm^{-3}) and manganese acetate (0.1 mol dm^{-3}) was used as the electrolyte. Then MO was electrodeposited on the pretreated CC (1 × 1.5 cm^2) via a constant current density of 0.5A cm^{-2} in three-electrode system. Electrodes with the electrodeposition time of 40 and 60 min were named as the MO electrode and MO-P electrode, respectively. After the electrodeposition, the electrodes were washed with ultrapure water and dried at 60 °C for 6 h. The mass loading of MO on the electrodes were estimated to be 1.7 mg (MO electrode) and 2.4 mg (MO-P) electrode.

2.3. Synthesis of PPy/MO electrode

The pyrrole (Py) monomer was distilled before use. In a typical process, a solution of 0.2 mol dm^{-3} p-TSA containing 1% (V: V) Py monomer was prepared. Then the MO-P electrode was immersed into 30 ml above mixture solution. The polymerization of pyrrole monomer was accelerated by the Mn^{4+}, Mn^{3+} and H^+ catalysis. Finally, the PPy film was deposited on the surface of the manganese oxide for 10 s (PPy/MO-10), 50 s (PPy/MO-50), 100 s (PPy/MO-100), 200 s (PPy/MO-200), 300 s (PPy/MO-300) with the p-TSA dopant. The prepared samples were washed with the ultrapure water and dried at 60 °C for a night, and the mass loading of active material was about 2.1 mg, 2.0 mg, 1.9 mg, 2.0 mg, 2.1 mg, respectively. In order to further investigated the effect of p-TSA to MO electrode, we prepared another acid treatment manganese oxide (ATMO) electrode through the identical method using the same solution without pyrrole monomer. And the mass loading of the ATMO was about 2.3 mg after 100 s acid treatment.

2.4. Structure and morphology characterization

The morphologies and structures of MO, ATMO, PPy/MO were characterized by field emission scanning electron microscopy (FE-SEM, Hitachi S-4800) and transmission electron microscopic (TEM, FEI Tecnai F30, operated at 300 kV). XRD was performed on a SIEMENS D5000 X-ray diffractometer using Cu Kα irradiation (λ=0.15418 nm). Raman spectra was conducted on a micro-Raman spectroscope (JY-HR800, y532 nm wavelength YAG laser). The XPS was carried out on a multifunctional X-ray photoelectron spectroscope (XPS, PHI-5702, Mg Ka X-ray, 1253.6 eV).

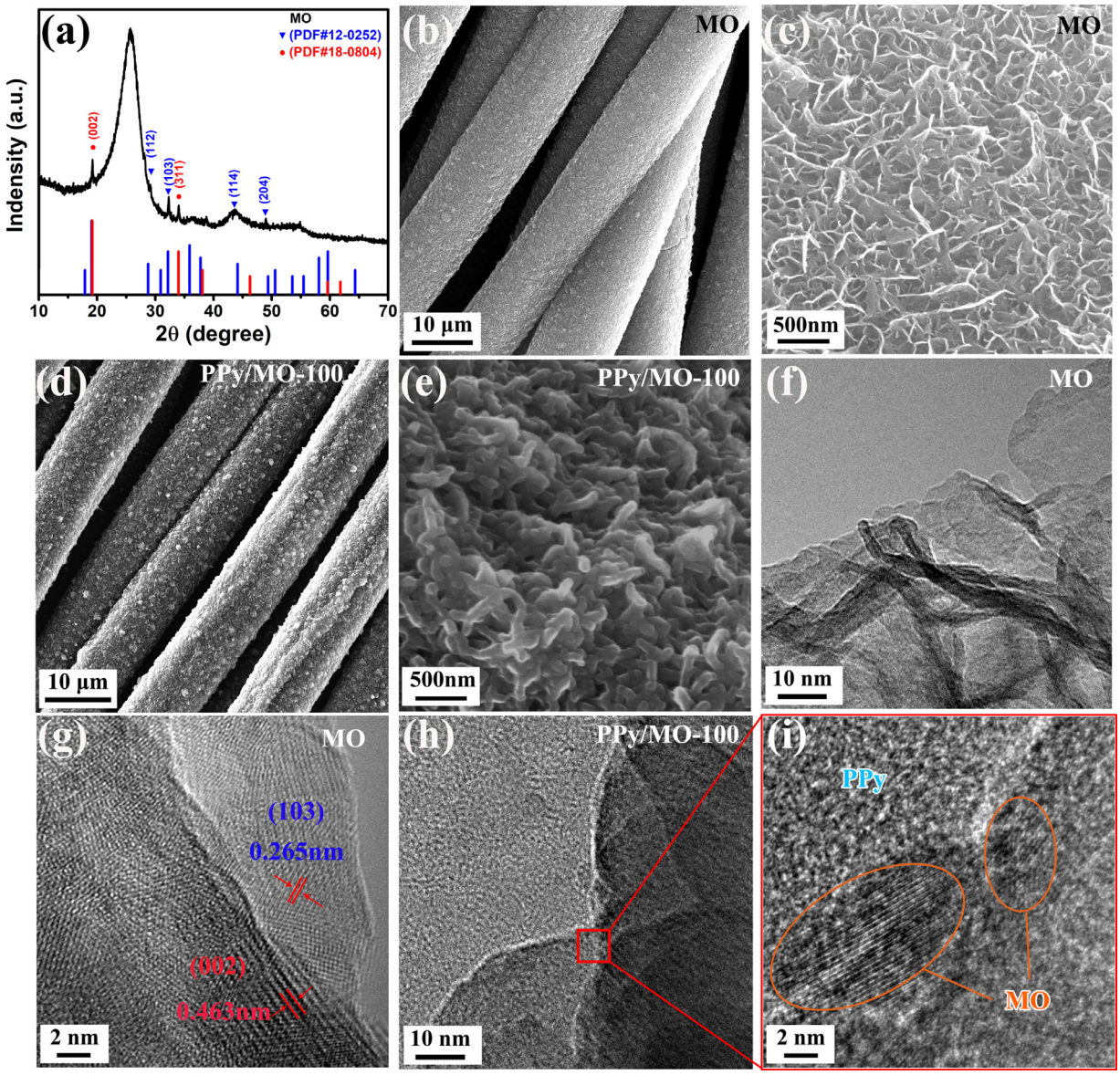

Fig. 1. (a) XRD pattern of MO electrode, SEM images for (b, c) MO and (d, e) PPy/MO-100 electrodes, TEM and HRTEM images for (f, g) MO and (h, i) PPy/MO-100.

2.5. Electrochemical property measurements

All the electrochemical tests for electrodes were carried out in 1 mol dm^{-3} Na_2SO_4 electrolyte with SCE as reference electrode and platinum plate as counter electrode. The three-electrode system was used in Cyclic voltammetry (CV), galvanostatic charge/discharge (GCD) and electrochemical impedance spectroscopy (EIS) on electrochemical workstations (CHI660E, CH Instruments Inc. Shanghai and Autolab PGSTAT 302 N). CV measurements were tested at the fixed potential range between −0.5–0.5 vs SCE/V with the different scan rates from 10 mV s^{-1} to 300 mV s^{-1}. GCD measurements were conducted at the potential range from −0.5 to 0.5 vs SCE/V under the various current density of 0.5 A g^{-1} to 10 A g^{-1}. CV and GCD tests were both carried out under the room temperature (about 23 °C). EIS measurements were performed with amplitude of 5 mV in the frequency from 100 kHz to 0.01 Hz at an open circuit potential. The long-term cycle was carried out through LANHE battery test system (CT3001A). The specific capacitance was calculated from GCD curves according to the formula: $C = (I\Delta t)/(m\Delta V)$, where I is the constant discharge current, Δt is the discharge time, m is the net mass of the active material of the electrode and ΔV is the working potential window.

3. Results and discussion

XRD pattern of the MO electrode shown in Fig. 1**(a)** can be well indexed to hydrohausmannite (JCPDS No:12–0252) and β-MnOOH (JCPDS No:18–0804). The broad peak at 26 ° is attribute to the substrate CC. MO shows a uniform flower-like morphology (Fig. 1**(b)** and **(c)**). After *in-situ* polymerization for 100 s (Fig. 1**(d) and (e)**), MO was evenly covered by PPy coating. PPy film are thicker and denser with increasing polymerization time ((**Fig. S1**)). TEM image of MO (Fig. 1**(f)**) well agrees with SEM results (Fig. 1**(c)**). The lattice space of 0.463 and 0.265 nm (Fig. 1**(g)**) corresponds to the (002) and (103) plane of β-MnOOH and hydrohausmannite, respectively. TEM image of PPy/MO-100 (Fig. 1**(h) and (i)**) further confirms that amorphous PPy film is deposited on MO. N and S element from p-TSA dopant in PPy uniformly distributed in PPy/MO-100 (**Fig. S2**), indicating a uniform growth of PPy.

Mn dissolution occurred during PPy polymerization since O element decreases and Mn element is hardly seen in the superficial

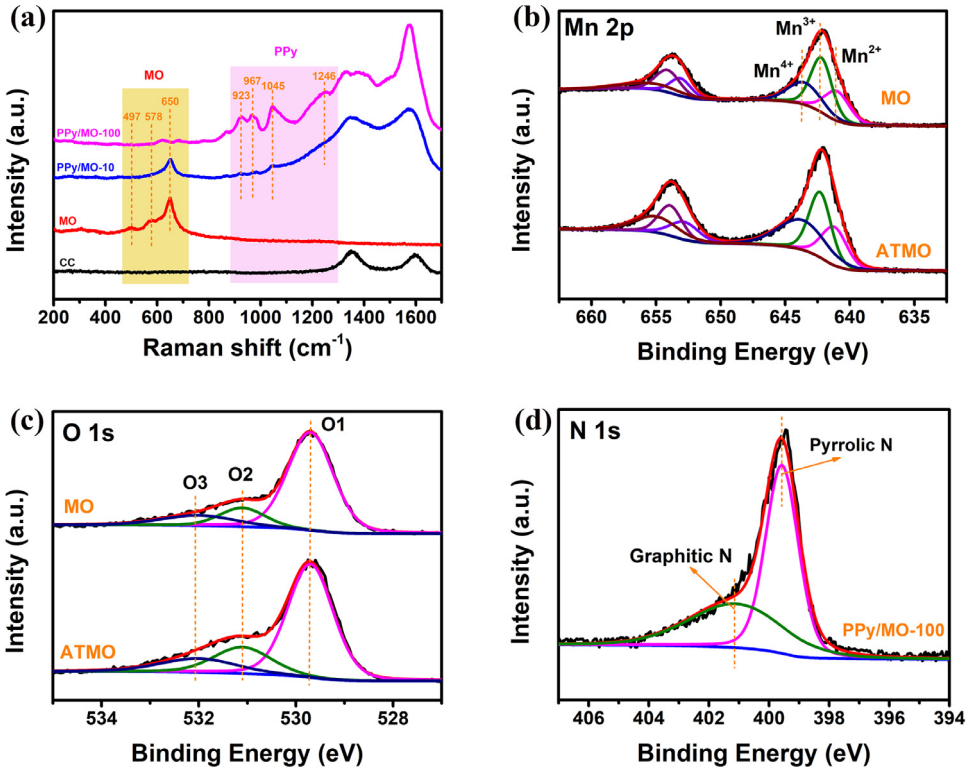

Fig. 2. (a) Raman spectra of CC, MO, PPy/MO-10 and PPy/MO-100 electrodes. (b) Mn 2p, (c) O 1 s XPS spectra of MO and ATMO electrodes, and (d) N 1 s spectra of PPy/MO-100 electrode.

region (**Fig. S2**). Thus, the actual polymerization process is that disproportionation reaction of Mn^{3+} Eq. (1)) in MO took place first under acid environment [42], then followed by polymerization of PPy (Eqs. (2)–((4)) [43] using Mn^{4+} as oxidant.

$$2Mn^{3+} + 2H_2O \leftrightarrow MnO_2 + Mn^{2+} + 4H^+ \quad (1)$$

$$n\mathrm{Py} \rightarrow (Py^{0.33+})n + 2nH^+ + 2.33ne^- \quad (2)$$

$$MnO_2 + 4H^+ + 2e\text{-} \rightarrow Mn^{2+} + 2H_2O \quad (3)$$

$$7n\mathrm{MnO_2} + 16n\mathrm{H^+} + 6n\mathrm{Py} \rightarrow 7\mathrm{Mn^{2+}} + 14n\mathrm{H_2O} + 6(Py^{0.33+}) \quad (4)$$

Typical bonds in Raman spectrum (**Fig. 2(a)**) around 1360 cm^{-1} (D band) and 1600 cm^{-1} (G bond) of CC comes from the in-plane bonds stretching motion of sp^2 C atom (E_2g phonon) at the Brillouin zone center and breathing modes of rings or K-point phonons of A_{1g} symmetry, respectively [44]. They are almost invisible in MO sample due to the thick and dense MO layer. For MO sample, the peaks observed at about 497 cm^{-1}, 578 cm^{-1}, 650 cm^{-1} ascribe to three typical vibrational bonds of manganese oxides, and the sharp peak located at 650 cm^{-1} is ascribe to the characterization of spinel structure. The band at about 578 cm^{-1} and 497 cm^{-1} can be assigned to two types of deformation modes of Mn-O-Mn chain in the basal plane of MnO_6 octahedral lattice [45]. This also confirms the mixed phase nature of MO.

For PPy/MO-10, the peaks at 923, 967 and 1045 cm^{-1} attribute to the C-H out-of-plane deformation, ring deformation, and C-H in-plane deformation, respectively [46]. This indicates that PPy has been synthesized on MO. Besides the peaks, another peak at 1246 cm^{-1} appeared in PPy/MO-100, which was assigned to the N-H in-plane deformation. The sharp peak at 650 cm^{-1} was invisible because PPy film has fully covered MO. Raman spectrum of PPy/MO electrodes with different polymerization time (**Fig. S3**) shows that the PPy bonds at 1246 cm^{-1} is the most obvious in PPy/MO-100. This might be ascribed to that shorter and longer polymerization time both result in lower polymerization degree due to lower amount of PPy and oxidant concentration, respectively.

Fig. 2(b) shows the Mn 2p XPS spectrum of MO and a referential ATMO electrodes, and no Mn signal is detected for PPy/MO-100 due to PPy film (**Fig. S4**). The six peaks at about 641.2 eV (653.3 eV), 642.4 eV (654.3 eV) and 643.7 eV (655.5 eV) were attributed to the Mn^{2+}, Mn^{3+} and Mn^{4+}, respectively [47]. Concentration of Mn^{2+}, Mn^{3+} and Mn^{4+} in MO were estimated to be 28%, 45% and 27%, while ATMO has almost the same concentration of Mn^{2+} (26%), but lower concentration of Mn^{3+} (37%) and higher concentration of Mn^{4+} (37%). This is because in ATMO Mn^{4+} and soluble Mn^{2+} are generated due to disproportionation reaction of Mn^{3+} during polymerization in acid environment. O 1 s XPS spectra of MO and ATMO are shown in **Fig. 2(c)**. Typically, O1 at 529.8 eV is assigned to the metal-oxygen bonds, O2 at 531.4 eV represents the oxygen in H-O groups, and O3 at 532.0 eV corresponds to the high-binding energy peak from surface oxygen defect species [48]. ATMO has higher proportion of O2 (20%) compared with MO (14%), which demonstrates that the residual H^+ are absorbed on ATMO surface. The peaks at 399.8 eV and 401.1 eV in N 1 s spectrum of PPy/MO-100 (**Fig. 2(d)**) correspond to pyrrolic N (-NH- bond) and graphitic N (C-N bond) [49,50], respectively. This also confirms that PPy was successfully synthesized on MO, corresponding to SEM result (**Fig. 1(d)**). Two peaks of S element in full XPS spectra of PPy/MO-100 (**Fig. S4**) prove the successful doping of PPy by p-TSA.

CV of MO (**Fig. 3(a)**) shows two peaks at −0.1 vs SCE/V and −0.33 vs SCE/V corresponding to the insertion/extraction of Na^+, and this process is highly irreversible as the peak area and position are altering during CV cycling. ATMO electrode has the same reaction at the same potential (**Fig. S5**), but the peaks are blunt because of more Mn^{4+} and active sites resulting from the dispropor-

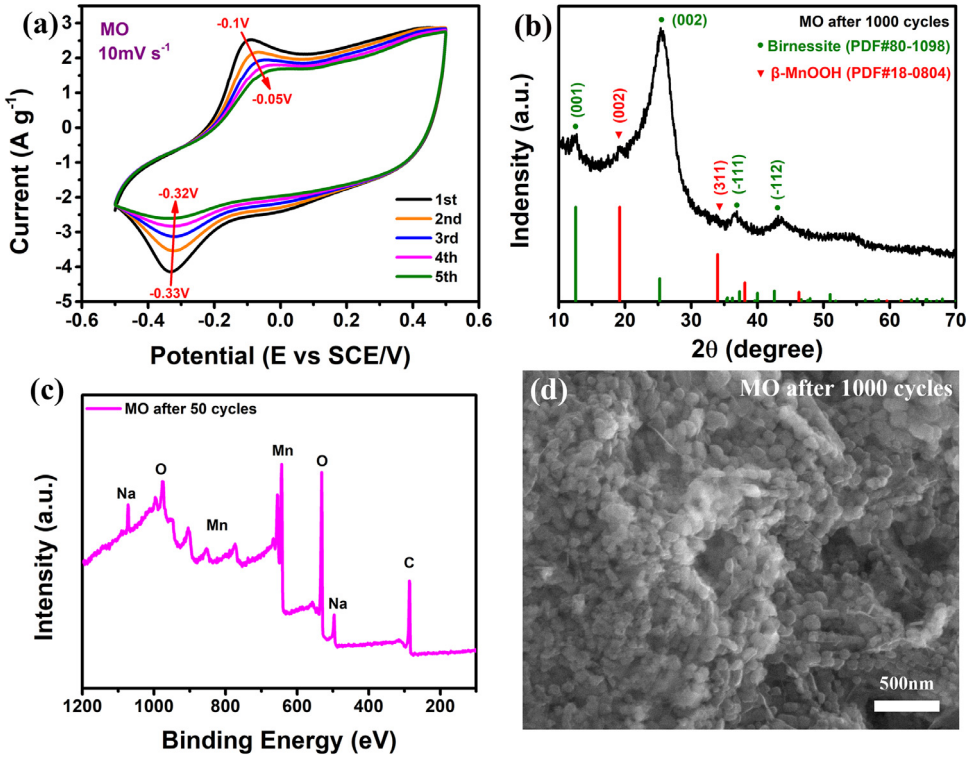

Fig. 3. (a) The first five CV profiles for MO at 10 mV s^{-1}; (b) The XRD pattern of MO electrode after 1000 cycles; (c) Full XPS spectrum of MO after 50 cycles; (d) SEM image of MO after 1000 GCD cycles at 10 A g^{-1}.

tionated reaction of Mn^{3+} and dissolution of Mn^{2+}. The reactions of MO electrodes during charge/discharge process can be described as [51–53]:

$$Mn_3O_4 \rightarrow Na_\delta MnO_x \bullet nH_2O \text{ (birnessite)} \quad (5)$$

$$MnO_2 + \delta Na^+ + \delta_e{}^- \leftrightarrow MnOONa \quad (6)$$

$$MnOOH \leftrightarrow MnO_2 + H^+ + e^- \quad (7)$$

$$MnO_x(OH)_y + \delta_H{}^+ + \delta_e{}^- \leftrightarrow MnO_{x\text{-}\delta}(OH)_{y+\delta} \quad (8)$$

$$Na_\delta MnO_x \bullet nH_2O + yH^+ + zNa^+ + (y+z)e^- \leftrightarrow Na_{\delta+z}MnO_x \bullet nH_2O \quad (9)$$

Where $MnO_x(OH)_y$, $MnO_{x\text{-}\delta}(OH)_{y+\delta}$ represent Mn_3O_4 under the higher and lower oxidation states, respectively. Eqs. (5) – (8) are the mainly energy storage processes.

Eq. (5) is a complicated and irreversible process corresponding to the two redox peaks, and represents the phase transformation to birnessite since the adsorption of solvated cations can result in a lower energy state [53]. XRD pattern of MO after 1000 cycles (**Fig. 3(b)**) confirms the phase transformation from MO to birnessite, since the diagnose peak of birnessite (001) plane can be clearly identified. Besides, full XPS spectra of MO after 50 cycles (**Fig. 3(c)**) shows a distinct peak of Na element, indicating that Na^+ participates in the energy storage process and part of Na ions were stuck into the bulk of MO. Eq. (6) was a reversible redox transition through the exchange of Na ions on the active sites of MO electrode. The sharp peak of typical (002) plane (**Fig. 3(b)**) of MnOOH were replaced by a hump, indicating that the MnOOH also took part in the energy storage process, as depicted by Eq. (7). O1s spectrum (**Fig. S6(a)**) shows an increased proportion of O2 from 14% to 26%, indicating the increase of O-H bonds due to the H^+ insertion, so H^+ also involves in the energy storage process as described by Eq. (8). Eq. (9) corresponds to the charge transfer process after the phase transformation from MO to birnessite. Therefore, the energy storage mechanism of MO is a co-intercalation/adsorption mechanism of Na^+ and H^+ accompanied by irreversible phase transformation from MO to birnessite in the early stage.

Moreover, Mn dissolution caused by disproportionation reaction of Mn^{3+} and structural collapse of MO are also confirmed during energy storage process. Mn2p spectrum after 50 cycles (**Fig. S6(b)**) reveals the fraction of Mn^{2+}, Mn^{3+} and Mn^{4+} was estimated to be 29%, 41% and 30%, respectively. The average valence of Mn ions (3.01 calculated according to (**Fig. S6(b)**) after 50 cycles was slightly higher than initial MO electrode (2.99), indicating the dissolution of Mn ions due to the intercalated Na^+ and H^+ ions and electrical neutral requirement of the overall electrode. Therefore, the energy storage process accompanied with the reduction of the valence state for Mn ion. Part of Mn^{2+} ions were dissolved in the electrolyte, which caused the rapid deterioration of electrochemical performance. This result was quite similar to the energy storage mechanism of MnO_2 electrode under negative potential reported by Ataherian's group [30]. Besides, SEM images of MO after 1000 cycles (**Fig. 3(d)**) show a dramatic morphology change (structural collapse) of MO.

To enhance the electrochemical property at negative potentials, PPy film is *in-situ* polymerized on MO surface in acid environment with different polymerization time. CV curves of all PPy/MO electrodes at 10 mV s^{-1} (**Fig. S7**) reveals that PPy/MO-100 has the largest CV area, indicated the highest specific capacitance. Comparing CV of PPy/MO-10 (**Fig. 4(a)**), PPy/MO-50 (**Fig. S8**) and PPy/MO-100 (**Fig. 4(b)**), the two redox peaks of MO become weaker because PPy film hinders more Na^+ from passing through. CV of PPy/MO-100 (**Fig. 4(c)**) has a typical enlarged rectangular shape, revealing the ideal capacitive performance and higher specific capacitance. No redox peak is detected because Na^+ cannot pass

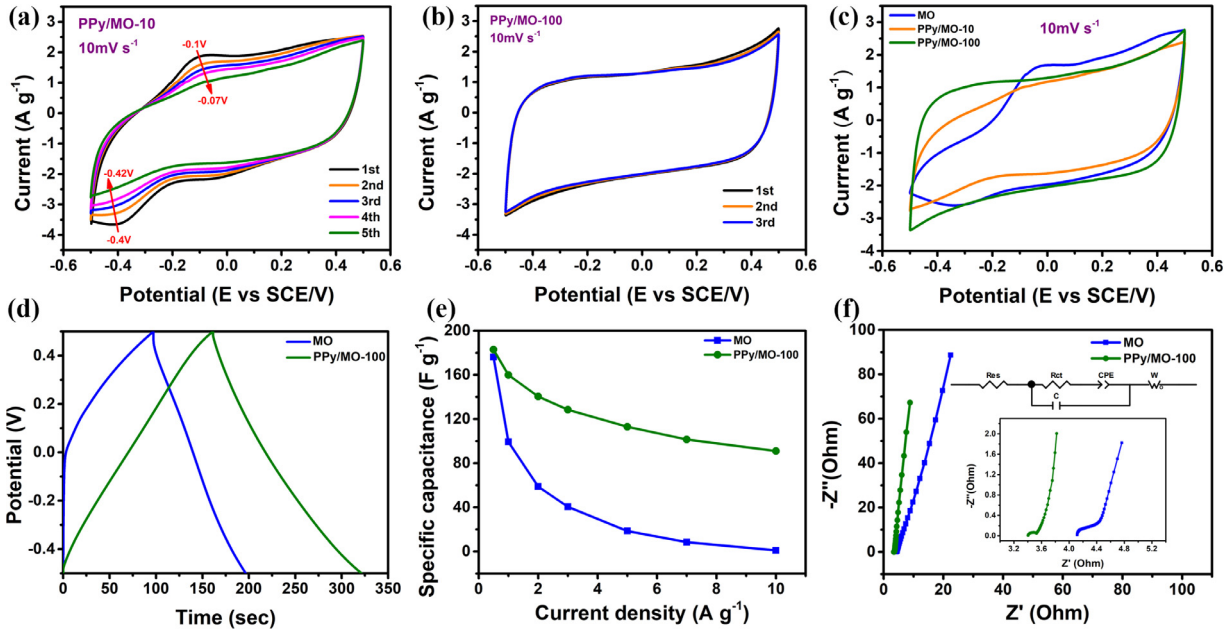

Fig. 4. Electrochemical performance characterizations for MO and PPy/MO electrode materials: (a) The first five CV profiles for PPy/MO-1 electrode at 10 mV s^{-1}; (b) The first three CV profiles for PPy/MO-100 electrode at 10 mV s^{-1}; (c) CV curves at 10 mV s^{-1} after 10 cycles; (d) GCD curves at a 1 A g^{-1}; (e) Specific capacitance of MO and PPy/MO-100 electrodes from 0.5 A g^{-1} to 10 A g^{-1}; (f) Nyquist plots, inset of (f) shows the magnified high-frequency range.

through, demonstrating that the irreversible redox reaction and phase transformation caused by Na^+ are sufficiently suppressed. Thus, the charge storage mechanism is mainly attribute to the intercalation/extraction of H^+ in MO (Eq. (8)) and doping/dedoping of anions in PPy film [39].

$$[PPy^+]D^- + e^- \leftrightarrow PPy^0 + D^- \quad (10)$$

where D represents the possible anions (SO_4^{2-} and p-TS^-) in the bulk of PPy and electrolyte. Therefore, anions are also involved in the energy storage process when PPy is introduced.

GCD profile of PPy/MO-100 (**Fig. 4(d)**) shows a highly linear and symmetrical curve with the longest discharge time, presenting the better pseudocapacitive behaviors and highest specific capacitance of 183F g^{-1} at 0.5A g^{-1} compared with other electrodes (**Fig. S9**). The specific capacitance of PPy/MO-100 in our work was higher than the hydrohausmannite electrode (37.5 F g^{-1} at 0.5A g^{-1} with the potential range of 0~0.8 vs SCE/V) [19], γ-Mn_3O_4 electrode (147 F g^{-1} at 0.1A g^{-1} with the potential range of −0.2~0.8 vs SCE/V) [54] and MnOOH electrode (131.9 F g^{-1} at 0.5A g^{-1} with the potential range of 0~1.0 vs SCE/V) [55] in 1 mol dm^{-3} $NaSO_4$ electrolyte. Shorter and longer polymerization time (than 100 s) can both result in lower specific capacitance because of lower ionic conductivity of MO and longer ion diffusion path in PPy, respectively. High polymerization degree of PPy/MO-100 suggested by Raman spectra (**Fig. S3**) may also contribute to the high specific capacitance.

Rate capability of MO and PPy/MO-100 electrodes are shown in **Fig. 4(e)**. The specific capacitance of PPy/MO-100 is 91 F g^{-1} at 10 A g^{-1}, much larger than that of MO (10 F g^{-1}). This suggests the PPy coating on MO can dramatically increase its rate capability. **Fig. S10** shows the rate capability of various PPy/MO electrodes at different current densities. PPy/MO-100 shows the most balanced performance with the highest specific capacitance and excellent rate capability. Nyquist plots of MO and PPy/MO-100 and equivalent circuit are shown in **Fig. 4(f),** and the parameters of equivalent circuit are summarized in **Table S1**. PPy/MO-100 electrode shows almost vertical inclination in low frequency region, indicating an ideal capacitive behavior, and it also has the lower equivalent series resistance (R_{es}) of 3.43 Ω with lower charge transfer resistance (R_{ct}) of 0.10 Ω. This indicates that the presence of PPy significantly increases the electrical conductivity and accelerates charge transfer process, which greatly raises the rate capability.

Capacitance retention (**Fig. S11**) of PPy/MO-10, PPy/MO-50, PPy/MO-100, PPy/MO-200, PPy/MO-300 is about 73%, 85.7%, 93.7%, 98.8% and 96.2% after 1000 GCD cycles at 10 A/g with almost 100% coulombic efficiency, respectively. Cycling stability mainly increase with polymerization time. Low cycling stability of PPy/MO-10 and PPy/MO-50 could be ascribed to PPy volume expansion and interfacial structural failure. PPy film tent to attract anions from the electrolyte during the charge process and release the anions back to the electrolyte in the reverse discharge process, causing swell and shrink, respectively [22]. SEM image of PPy/MO-100 after 1000 cycles (**Fig. S12**) shows an unchanged surface morphology without visible damage. Good integrity of electrode surface demonstrated that the PPy film can protect the initial MO from phase transformation and structural collapse. To further investigate the stability of PPy film, full XPS spectra of PPy/MO-100 electrodes after 1000 cycles was shown in **Fig. S13**. The characteristic peaks of N and S element were consistent with the original PPy film, indicating superior physicochemical stable property. It should be noted that the characteristic peaks of Mn ion were still invisible but a weak peak of Na ion was appeared, confirming that part of Na ions was trapped in the PPy film during the charge/discharge process and the dissolution of Mn ions was suppressed. Long-terms cycling stability of PPy/MO-100 electrode was shown in **Fig. S14**. The specific capacitance still maintains 77.7% after 4500 GCD cycles, which proves that the PPy film have excellent electrochemical stability.

Capacitive contribution to the overall specific capacitance of PPy/MO-100 are much higher than that of MO at various scan rates (**Fig. S15**), calculated according to previous reported method [47]. Capacitive contribution of PPy/MO-100 is about 50%, and only 27% for MO at 100 mV s^{-1}. On one hand, PPy film prevents irreversible redox reaction and phase transformation by hindering Na^+ from insertion/extraction in MO, which reduces specific capacitance to

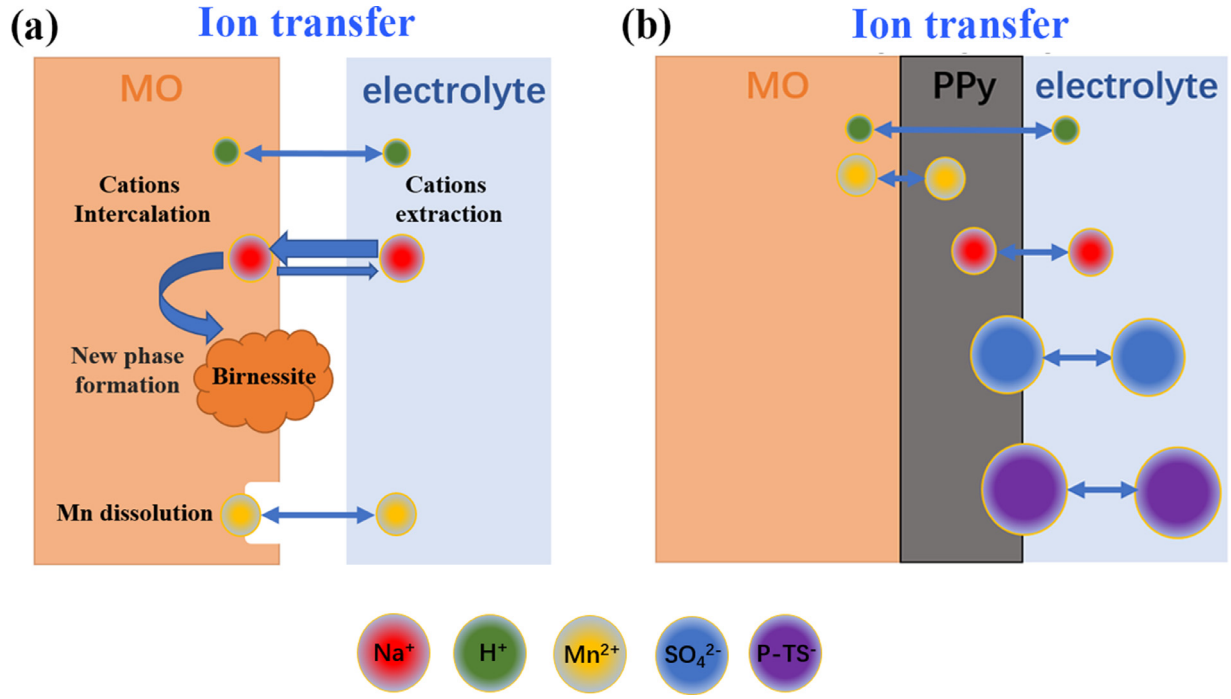

Fig. 5. Schematic illustration of energy storage mechanism of (a) MO and (b) PPy/MO-100 electrode.

some extent. On the other, PPy also provides capacitive capacitance itself and involves anions (SO_4^{2-} and p-TS^-) in the energy storage process, thus greatly increases specific capacitance.

The schematic illustration of energy storage mechanism is shown in **Fig. 5**. In summary, better capacitive performance of PPy/MO-100 mainly attributes to the following four aspects. Firstly, PPy film with appropriate polymerization time (or thickness) can allow only H^+ to pass through and hinder the irreversible phase transformation caused by Na^+ insertion, and thus can protect the pristine MO structure and morphology. Secondly, since PPy film isolates MO and electrolyte, it can also prevent Mn^{2+} from dissolving into electrolyte, suppress disproportionation reaction, and thus enhances the cycling stability. Zhu et al. has used the PPy film as a barrier to restraint the dissolution of MnO_2 during the discharge process [42], which is consistent with our results. Thirdly, PPy film can notably raising the conductivity of composite electrode and provide highly conductive pathways for rapid charge transfer, which can greatly increase the rate capability. This result was similar to the investigation of PPy film that reported by Bi's group [41]. Finally, besides cations (H^+ and Na^+), PPy film also introduces anions (SO_4^{2-} and p-TS^-) into the energy storage process, which great promotes the overall specific capacitance. When the polymerization time is too long, PPy film will hinder the pass of H^+ and undermines the utilization of MO, resulting in a lower specific capacitance.

4. Conclusions

Co-intercalation mechanism of H^+ and Na^+ are involved in the charge storage process of hydrohausmannite under negative potential (−0.5~0.5 vs SCE/V). Irreversible redox reaction and phase transformation to birnessite caused by Na^+ can result in performance fading and structure collapse. After *in-situ* polymerization of PPy film on MO surface in acid environment for 100 s, the PPy/MO-100 electrode shows a greatly promoted specific capacitance (183 F g^{-1} at 0.5 A g^{-1}), enhanced rate capability (91 F g^{-1} at 10 A g^{-1}, about 10 times of MO), and excellent cycling stability (93.7% capacitance retention after 1000 cycles and 77.7% capacitance retention after 4500 cycles at 10 A g^{-1}). The promoted performance is mainly ascribed to four aspects: Firstly, PPy films with appropriate polymerization time (or thickness) can allow H^+ to pass and block Na^+, so that the irreversible phase transformation is hindered and the structure and morphology of electrode is protected. Secondly, PPy film can also prevent Mn^{2+} from dissolving into electrolyte, so the disproportionation reaction is suppressed and cycling stability is greatly enhanced. Thirdly, PPy film can improve the conductivity of the electrode, which notably accelerates the charge transfer process and elevates the rate capability. Fourthly, besides cations (H^+ and Na^+), anions (SO_4^{2-} and p-TS^-) also participate in energy storage process after PPy coating, so the specific capacitance is greatly promoted.

Declaration of Competing Interest

The authors declare no competing financial interest.

Credit authorship contribution statement

Yan Zhuang: Data curation, Writing - original draft. **Qiangqiang Niu:** Investigation. **Wenjie Wu:** Investigation. **De Yan:** Conceptualization, Writing - review & editing, Formal analysis, Funding acquisition. **Juanjuan Huang:** Writing - review & editing. **Shanglong Peng:** Writing - review & editing. **Jun Wang:** Writing - review & editing. **Renfu Zhuo:** Writing - review & editing. **Zhiguo Wu:** Writing - review & editing. **Guozhong Cao:** Formal analysis, Writing - review & editing.

Acknowledgments

This research work is financially supported by the National Natural Science Foundation of China (Grant No. 11204114, 61376011, 51402141, 61604086), the Fundamental Research Funds for the Central Universities (Grant No. lzujbky-2017–175, lzujbky-2018–119, lzujbky-2018-ct08), the Natural Science Foundation of Gansu (Grant No.17JR5RA203, 17JR5RA198), Lanzhou Chengguan District Scientific Research Foundation (2018KJGG0052),

Shenzhen Science and Technology Innovation Committee (No. JCYJ20170818155813437), Key Areas Scientific and Technological Research Projects in Xinjiang Production and Construction Corps (No. 2018AB004), and the National Science Foundation (CBET-1803256).

Supplementary materials

Supplementary material associated with this article can be found, in the online version, at doi:10.1016/j.electacta.2021.137989.

Reference

[1] S. Wang, L. Gai, J. Zhou, H. Jiang, Y. Sun, H. Zhang, Thermal cyclodebromination of polybromopyrroles to polymer with high performance for supercapacitor, J. Phys. Chem. C 119 (2015) 3881–3891.

[2] S. Ramesh, H.M. Yadav, K. Karuppasamy, D. Vikraman, H.-S. Kim, J.-H. Kim, H.S. Kim, Fabrication of manganese oxide@nitrogen doped graphene oxide/polypyrrole (MnO_2@NGO/PPy) hybrid composite electrodes for energy storage devices, J. Mater. Res. Technol. 8 (2019) 4227–4238.

[3] M.H. Bai, L.J. Bian, Y. Song, X.X. Liu, Electrochemical codeposition of vanadium oxide and polypyrrole for high-performance supercapacitor with high working voltage, ACS Appl. Mater. Interfaces 6 (2014) 12656–12664.

[4] Z. Zhang, K. Chi, F. Xiao, S. Wang, Advanced solid-state asymmetric supercapacitors based on 3D graphene/MnO_2 and graphene/polypyrrole hybrid architectures, J. Mater. Chem. A 3 (2015) 12828–12835.

[5] Q. Qu, Y. Zhu, X. Gao, Y. Wu, Core-shell structure of polypyrrole grown on V_2O_5 nanoribbon as high performance anode material for supercapacitors, Adv. Energy Mater. 2 (2012) 950–955.

[6] Y. Zhu, E. Liu, Z. Luo, T. Hu, T. Liu, Z. Li, Q. Zhao, A hydroquinone redox electrolyte for polyaniline/SnO_2 supercapacitors, Electrochim. Acta 118 (2014) 106–111.

[7] H. Wang, Y. Liang, T. Mirfakhrai, Z. Chen, H.S. Casalongue, H. Dai, Advanced asymmetrical supercapacitors based on graphene hybrid materials, Nano Res. 4 (2011) 729–736.

[8] S. Korkmaz, F. Meydaneri Tezel, İ.A. Kariper, Synthesis and characterization of GO/IrO_2 thin film supercapacitor, J. Alloy. Compd. 754 (2018) 14–25.

[9] D. Xiong, X. Li, Z. Bai, J. Li, H. Shan, L. Fan, C. Long, D. Li, X. Lu, Rational design of hybrid Co_3O_4/graphene films: free-standing flexible electrodes for high performance supercapacitors, Electrochim. Acta 259 (2018) 338–347.

[10] Z.H. Huang, Y. Song, D.Y. Feng, Z. Sun, X. Sun, X.X. Liu, High mass loading MnO_2 with hierarchical nanostructures for supercapacitors, ACS Nano 12 (2018) 3557–3567.

[11] F. Qin, X. Tian, Z. Guo, W. Shen, Asphaltene-based porous carbon nanosheet as electrode for supercapacitor, ACS Sustain. Chem. Eng. 6 (2018) 15708–15719.

[12] X. Wang, T.S. Mathis, K. Li, Z. Lin, L. Vlcek, T. Torita, N.C. Osti, C. Hatter, P. Urbankowski, A. Sarycheva, M. Tyagi, E. Mamontov, P. Simon, Y. Gogotsi, Influences from solvents on charge storage in titanium carbide MXenes, Nat. Energy 4 (2019) 241–248.

[13] Y. Cao, Y. Xiao, Y. Gong, C. Wang, F. Li, One-pot synthesis of MnOOH nanorods on graphene for asymmetric supercapacitors, Electrochim. Acta 127 (2014) 200–207.

[14] P.T.M. Bui, J.H. Song, Z.Y. Li, M.S. Akhtar, O.B. Yang, Low temperature solution processed Mn_3O_4 nanoparticles: enhanced performance of electrochemical supercapacitors, J. Alloy. Compd. 694 (2017) 560–567.

[15] J. Xu, Y. Sun, M. Lu, L. Wang, J. Zhang, J. Qian, E.J. Kim, Fabrication of porous Mn_2O_3 microsheet arrays on nickel foam as high–rate electrodes for supercapacitors, J. Alloy. Compd. 717 (2017) 108–115.

[16] G. Wang, L. Zhang, J. Zhang, A review of electrode materials for electrochemical supercapacitors, Chem. Soc. Rev. 41 (2012) 797–828.

[17] A.A. Radhiyah, M. Izan Izwan, V. Baiju, C. Kwok Feng, I. Jamil, R. Jose, Doubling of electrochemical parameters via the pre-intercalation of Na^+ in layered MnO_2 nanoflakes compared to α-MnO_2 nanorods, RSC Adv. 5 (2015) 9667–9673.

[18] D. Yan, Y. Li, Y. Liu, R. Zhuo, Z. Wu, B. Geng, J. Wang, P. Ren, P. Yan, Z. Geng, Hydrothermal synthesis and electrochemical properties of hexagonal hydrohausmannite plates as supercapacitor electrode material, Mater. Lett. 117 (2014) 62–65.

[19] J. Liang, Y. Chai, D. Li, M. Li, J. Lu, L. Li, M. Luo, Facile fabrication of plate-shaped hydrohausmannite as electrode material for supercapacitors, Appl. Surf. Sci. 414 (2017) 68–72.

[20] A.A. Vannathan, S. Maity, T. Kella, D. Shee, P.P. Das, S.S. Mal, *In situ* vanadophosphomolybdate impregnated into conducting polypyrrole for supercapacitor, Electrochim. Acta 364 (2020) 137286.

[21] J. Lee, H. Jeong, R. Lassarote Lavall, A. Busnaina, Y. Kim, Y.J. Jung, H. Lee, Polypyrrole films with micro/nanosphere shapes for electrodes of high-performance supercapacitors, ACS Appl. Mater. Interfaces 9 (2017) 33203–33211.

[22] Y. Huang, M. Zhu, Z. Pei, Y. Huang, H. Geng, C. Zhi, Extremely stable polypyrrole achieved via molecular ordering for highly flexible supercapacitors, ACS Appl. Mater. Interfaces 8 (2016) 2435–2440.

[23] H. Fu, Z.J. Du, W. Zou, H.Q. Li, C. Zhang, Carbon nanotube reinforced polypyrrole nanowire network as a high-performance supercapacitor electrode, J. Mater. Chem. A 1 (2013) 14943–14950.

[24] A. Kumar, R.K. Singh, H.K. Singh, P. Srivastava, R. Singh, Enhanced capacitance and stability of p-toluenesulfonate doped polypyrrole/carbon composite for electrode application in electrochemical capacitors, J. Power Sour. 246 (2014) 800–807.

[25] Z.H. Dong, Y.L. Wei, W. Shi, G.A. Zhang, Characterisation of doped polypyrrole/manganese oxide nanocomposite for supercapacitor electrodes, Mater. Chem. Phys. 131 (2011) 529–534.

[26] C.J. Raj, B.C. Kim, W.J. Cho, W.G. Lee, S.D. Jung, Y.H. Kim, S.Y. Park, K.H. Yu, Highly flexible and planar supercapacitors using graphite flakes/polypyrrole in polymer lapping film, ACS Appl. Mater. Interfaces 7 (2015) 13405–13414.

[27] C. Sun, X. Li, Z. Cai, F. Ge, Carbonized cotton fabric *in-situ* electrodeposition polypyrrole as high-performance flexible electrode for wearable supercapacitor, Electrochim. Acta 296 (2019) 617–626.

[28] J.-G. Wang, F. Kang, B. Wei, Engineering of MnO_2-based nanocomposites for high-performance supercapacitors, Prog. Mater. Sci. 74 (2015) 51–124.

[29] S. Sopčić, R. Peter, M. Petravić, Z. Mandić, New insights into the mechanism of pseudocapacitance deterioration in electrodeposited MnO_2 under negative potentials, J. Power Sour. 240 (2013) 252–257.

[30] F. Ataherian, K.T. Lee, N.L. Wu, Long-term electrochemical behaviors of manganese oxide aqueous electrochemical capacitor under reducing potentials, Electrochim. Acta 55 (2010) 7429–7435.

[31] Y.C. Hsieh, K.T. Lee, Y.P. Lin, N.L. Wu, S.W. Donne, Investigation on capacity fading of aqueous $MnO_2 \bullet nH_2O$ electrochemical capacitor, J. Power Sour. 177 (2008) 660–664.

[32] M. Li, J. Yu, X. Wang, Z. Yang, 3D porous MnO_2@carbon nanosheet synthesized from rambutan peel for high-performing supercapacitor electrodes materials, Appl. Surf. Sci. 530 (2020) 147230.

[33] W. Gong, B. Fugetsu, Q. Li, A.K. Vipin, T. Konishi, T. Ueki, I. Sakata, Z. Wang, M. Yu, L. Su, X. Zhang, M. Terrones, M. Endo, Improved supercapacitors by implanting ultra-long single-walled carbon nanotubes into manganese oxide domains, J. Power Sour. 479 (2020) 228795.

[34] G. Wu, X. Yang, C. Hou, Y. Li, Q. Zhang, H. Wang, High volumetric energy density asymmetric fibrous supercapacitors with coaxial structure based on graphene/MnO_2 hybrid fibers, ChemElectroChem 7 (2020) 4641–4648.

[35] Y. Huang, S. Bao, J. Lu, Flower-like MnO_2/polyaniline/hollow mesoporous silica as electrode for high-performance all-solid-state supercapacitors, J. Alloy. Compd. 845 (2020) 156192.

[36] G. Yang, X. Li, T. Chen, W. Gao, Y. Dai, X. Li, Self-supported PANI@MnO_2 coaxial nanowire network sponge as a binder free electrode for supercapacitors, J. Nanosci. Nanotechnol. 20 (2020) 4203–4209.

[37] P. Sen, S. Rana, A. De, Hierarchical design of rGO-PEDOT- δ-MnO_2 nanocomposite for supercapacitors, J. Electron. Mater. 49 (2019) 763–772.

[38] R. Malik, S. Lata, U. Soni, P. Rani, R.S. Malik, Carbon quantum dots intercalated in polypyrrole (PPy) thin electrodes for accelerated energy storage, Electrochim. Acta 364 (2020) 137281.

[39] W. He, C. Wang, F. Zhuge, X. Deng, X. Xu, T. Zhai, Flexible and high energy density asymmetrical supercapacitors based on core/shell conducting polymer nanowires/manganese dioxide nanoflakes, Nano Energy 35 (2017) 242–250.

[40] R.K. Sharma, A.C. Rastogi, S.B. Desu, Manganese oxide embedded polypyrrole nanocomposites for electrochemical supercapacitor, Electrochim. Acta 53 (2008) 7690–7695.

[41] W. Bi, J. Huang, M. Wang, E.P. Jahrman, G.T. Seidler, J. Wang, Y. Wu, G. Gao, G. Wu, G. Cao, V_2O_5–Conductive polymer nanocables with built-in local electric field derived from interfacial oxygen vacancies for high energy density supercapacitors, J. Mater. Chem. A 7 (2019) 17966–17973.

[42] Q. Zhu, K. Liu, J. Zhou, H. Hu, W. Chen, Y. Yu, Design of a unique 3D-nanostructure to make MnO_2 work as supercapacitor material in acid environment, Chem. Eng. J. 321 (2017) 554–563.

[43] Y. Chen, X. Zhang, C. Xu, H. Xu, The fabrication of asymmetry supercapacitor based on MWCNTs/MnO_2/PPy composites, Electrochim. Acta 309 (2019) 424–431.

[44] T. Qin, B. Liu, Y. Wen, Z. Wang, X. Jiang, Z. Wan, S. Peng, G. Cao, D. He, Free-standing flexible graphene foams@polypyrrole@MnO_2 electrodes for high-performance supercapacitors, J. Mater. Chem. A 4 (2016) 9196–9203.

[45] T. Gao, H. Fjellvag, P. Norby, A comparison study on Raman scattering properties of alpha- and beta-MnO_2, Anal. Chim. Acta 648 (2009) 235–239.

[46] Z. Chen, L. Zheng, T. Zhu, Z. Ma, Y. Yang, C. Wei, L. Liu, X. Gong, All-solid-state flexible asymmetric supercapacitors fabricated by the binder-free hydrophilic carbon cloth@MnO_2 and hydrophilic carbon cloth@polypyrrole electrodes, Adv. Electron. Mater. 5 (2019) 1800721.

[47] T. Xiong, Z.G. Yu, H. Wu, Y. Du, Q. Xie, J. Chen, Y.W. Zhang, S.J. Pennycook, W.S.V. Lee, J. Xue, Defect engineering of oxygen-deficient manganese oxide to achieve high-performing aqueous zinc ion battery, Adv. Energy Mater. 9 (2019) 1803815.

[48] S. Lian, C. Sun, W. Xu, W. Huo, Y. Luo, K. Zhao, G. Yao, W. Xu, Y. Zhang, Z. Li, K. Yu, H. Zhao, H. Cheng, J. Zhang, L. Mai, Built-in oriented electric field facilitating durable Zn MnO_2 battery, Nano Energy 62 (2019) 79–84.

[49] Y. Wang, T. Liu, X. Lin, H. Chen, S. Chen, Z. Jiang, Y. Chen, J. Liu, J. Huang, M. Liu, Self-templated synthesis of hierarchically porous n-doped carbon derived from biomass for supercapacitors, ACS Sustain. Chem. Eng. 6 (2018) 13932–13939.

[50] C. Dong, L. Guo, H. Li, B. Zhang, X. Gao, F. Tian, Y. Qian, D. Wang, L. Xu, Rational fabrication of CoS_2/Co_4S_3@N-doped carbon microspheres as excellent cycling performance anode for half/full sodium ion batteries, Energy Storage Mater. 25 (2020) 679–686.

[51] J. Yang, X. Yang, Y.L. Zhong, J.Y. Ying, Porous MnO/Mn_3O_4 nanocomposites for electrochemical energy storage, Nano Energy 13 (2015) 702–708.

[52] L. Wang, G. Duan, S.M. Chen, X. Liu, Hydrothermally controlled synthesis of α-MnO_2, γ-MnOOH, and Mn_3O_4 nanomaterials with enhanced electrochemical properties, J. Alloy. Compd. 752 (2018) 123–132.
[53] P. Suktha, N. Phattharasupakun, P. Dittanet, M. Sawangphruk, Charge storage mechanisms of electrospun Mn_3O_4 nanofibres for high-performance supercapacitors, RSC Adv. 7 (2017) 9958–9963.
[54] Y. Fan, X. Zhang, Y. Liu, Q. Cai, J. Zhang, One-pot hydrothermal synthesis of Mn_3O_4/graphene nanocomposite for supercapacitors, Mater. Lett. 95 (2013) 153–156.
[55] Z. Li, H. Bao, X. Miao, X. Chen, A facile route to growth of gamma-MnOOH nanorods and electrochemical capacitance properties, J. Colloid Interface Sci. 357 (2011) 286–291.